Journal of Power Sources 196 (2011) 1826–1832

Contents lists available at ScienceDirect

Journal of Power Sources

journal homepage: www.elsevier.com/locate/jpowsour

# Nanostructured $La_{0.6}Sr_{0.4}Co_{0.8}Fe_{0.2}O_3$/$Y_{0.08}Zr_{0.92}O_{1.96}$/$La_{0.6}Sr_{0.4}Co_{0.8}Fe_{0.2}O_3$ (LSCF/YSZ/LSCF) symmetric thin film solid oxide fuel cells

Bo-Kuai Lai*, Kian Kerman, Shriram Ramanathan

*Harvard School of Engineering and Applied Sciences, Harvard University, Cambridge, MA 02138, USA*

ARTICLE INFO

*Article history:*
Received 4 August 2010
Accepted 21 September 2010
Available online 1 October 2010

*Keywords:*
LSCF
Solid oxide fuel cell
Cathode
Anode
Pt
Thin film

ABSTRACT

Functional all-oxide thin film micro-solid oxide fuel cells (μSOFCs) that are free of platinum (Pt) are discussed in this report. The μSOFCs, with widths of 160 μm, consist of thin film $La_{0.6}Sr_{0.4}Co_{0.8}Fe_{0.2}O_3$ (LSCF) as both the anode and cathode and $Y_{0.08}Zr_{0.92}O_{1.96}$ (YSZ) as the electrolyte. Open circuit voltage and peak power density at 545 °C are 0.18 V and 210 μW cm$^{-2}$, respectively. The LSCF anodes show good lattice and microstructure stability and do not form reaction products with YSZ. The all-oxide μSOFCs endure long-term stability testing at 500 °C for over 100 h, as manifested by stable membrane morphology and crack-free microstructure.

Published by Elsevier B.V.

## 1. Introduction

Micro-solid oxide fuel cells (μSOFCs) utilizing thin film components and fabricated on silicon platforms have been receiving increasing attention over the last decade [1–6]. Potential advantages include small form factor that could be relevant for portable energy applications requiring miniature power sources [1] and low-temperature functionality [3]. To date, majority of μSOFCs demonstrated use Pt as the anode material [1,3,6,7]. The limitation of Pt anodes, typically synthesized with a porous microstructure, is their cost and microstructural instability due to the Ostwald ripening and dewetting effect [6,7]. To be cost competitive and functionally reliable, reducing or eliminating Pt loading is of particular importance. From efforts in anode development for conventional SOFCs [8], electrocatalytic oxides appear to be promising Pt alternatives for microstructurally stable, affordable anodes for μSOFCs. In the past three decades, a plethora of work [8–12] has been carried out on exploring such oxides to replace Ni-YSZ cermet anodes. Most of the suitable oxides reported, such as $La_{0.75}Sr_{0.25}Cr_{0.5}Mn_{0.5}O_3$ [11], $La_xSr_{1-x}Co_yTi_{1-y}O_3$ [13], and $La_{0.8}Sr_{0.2}Sc_{0.2}Mn_{0.8}O_3$ [12], possess $ABO_3$ type perovskite structure. The perovskite structure is flexible with regards to doping various transition metals into A- and/or B-sites and can accommodate high oxygen deficiency, allowing the highly correlated ionic, electronic, and electrocatalytic properties to be delicately optimized [14–16]. Typically, power density of SOFCs using perovskite oxide anodes is lower than the SOFCs using Ni-YSZ anodes. For instance, Tao and Irvine [11] reported that SOFCs with 50-μm-thick $La_{0.75}Sr_{0.25}Cr_{0.5}Mn_{0.5}O_3$ anodes and Pt current collectors reach a power density of 300 mW cm$^{-2}$ at 900 °C when operated with wet 5% $H_2$ fuel.

In this report, we explore $La_{0.6}Sr_{0.4}Co_{0.8}Fe_{0.2}O_3$ (LSCF) as an anode material to demonstrate the feasibility of Pt-free, all-oxide μSOFCs. The rationale is the following: Firstly, although $La_xSr_{1-x}Co_yFe_{1-y}O_3$ is better studied as a cathode for intermediate-temperature SOFCs, it has also been implemented as anode in SOFCs [17,18] due to its capability of direct methane conversion [19–23]. Such capability is desirable for oxide anodes in μSOFCs because methane is more widely available and economically feasible in comparison with $H_2$. When fueled by methane, Fisher and Chuang [17] reported an OCV and power density of SOFCs with a $La_{0.6}Sr_{0.4}Co_{0.2}Fe_{0.8}O_3$ anode reach 1.0 V and 186 mW cm$^{-2}$ at 900 °C; no performance degradation was observed after 72 h of testing. Sin et al. [18] implemented a $La_{0.6}Sr_{0.4}Co_{0.2}Fe_{0.8}O_3$–$Ce_{0.8}Gd_{0.2}O_{1.9}$ (70 wt.%:30 wt.%) composite as the SOFC anode. OCV and power density of such SOFCs reach 0.82 V and 170 mW cm$^{-2}$, respectively, at 800 °C. After the testing, the anode did not show any structural degradation or carbon deposition.

Secondly, the possibility of using $La_xSr_{1-x}Co_yFe_{1-y}O_3$, or similar complex electrocatalytic oxides, as both the cathode and anode is intriguing because symmetric all-oxide SOFCs [12] have several potential advantages over their asymmetric Ni- or Pt-containing counterparts – namely, simplicity of fabrication, better strain/stress

* Corresponding author. Tel.: +1 617 497 4632; fax: +1 617 497 4627.
*E-mail address:* blai@seas.harvard.edu (B.-K. Lai).

0378-7753/$ – see front matter. Published by Elsevier B.V.
doi:10.1016/j.jpowsour.2010.09.066

and interface control to maintain microstructure stability, and potential elimination of anode poisoning by switching fuel and oxidant. Recently, Zheng et al. [12] have demonstrated symmetric SOFCs with $La_{0.8}Sr_{0.2}Sc_{0.2}Mn_{0.8}O_3$ as the cathode and anode. Power density of 310 mW cm$^{-2}$ was obtained at 900 °C when fueled with wet 5% $H_2$ fuel; Ag and/or Au were used as current collectors.

Thirdly, LSCF ultra-thin films have been recently optimized [24–28] in LSCF/YSZ/Pt μSOFCs. The optimized LSCF possesses compressive stresses within an appropriate range during thermal cycling [25,27,29–31], effectively avoiding crack formation and stress-related failures in μSOFCs. The crack prevention and stress management during fuel cell fabrication, thermal cycling, and long-term operation at high temperatures are extremely critical for reliable all-oxide μSOFCs because these μSOFC membranes are freestanding, stressed, and ultrathin (typically sub-μm). Successful implementation of LSCF anode in μSOFCs may also serve as a stepping stone for incorporating other perovskite oxides, such as $La_{0.75}Sr_{0.25}Cr_{0.5}Mn_{0.5}O_3$ [11], $La_xSr_{1-x}Co_yTi_{1-y}O_3$ [13], and $La_{0.8}Sr_{0.2}Sc_{0.2}Mn_{0.8}O_3$ [12]. Moreover, it may also open up possibilities of symmetric all-oxide μSOFCs and direct-methane μSOFCs. However, as pointed out by Weston and Metcalfe [21], thermomechanical instability of LSCF anodes could be a concern because high oxygen vacancy concentration could be generated in LSCF anode in reducing environment at elevated temperatures.

The goal of this report is to investigate LSCF thin films as an anode in μSOFCs, while also using identical LSCF thin films as the cathode and YSZ thin films as the electrolyte. The emphasis is on lattice and microstructure stability of thin-film LSCF anode and buckling deformation stability of sub-μm LSCF-YSZ-LSCF (referred to as LYL) μSOFC membranes. To the best of author's knowledge, all-oxide thin film μSOFCs have not been reported to date. Our results show that the microstructure of LSCF thin films is stable in a reducing environment under the conditions tested in this report. The corresponding all-oxide LYL μSOFCs exhibit remarkable thermomechanical stability, as manifested by stable buckling deformation and crack-free microstructure after over 100 h of long-term stability testing at 500 °C. Power densities of 125 and 210 μW cm$^{-2}$ at 420 and 545 °C, respectively, from these first-of-a-kind cells are encouraging despite significant resistive losses from the anode. We note that the performance could potentially be further improved with integrated current collectors and by optimization of anode microstructure.

## 2. Experimental

Deposition of 8% yttria-doped zirconia (YSZ) and $La_{0.6}Sr_{0.4}Co_{0.8}Fe_{0.2}O_3$ (LSCF) thin films was performed in 5 mTorr Ar and at substrate temperature of 500 °C by rf-sputtering from composite targets. Both as-deposited YSZ and LSCF thin films were crystalline. Target power used for YSZ and LSCF target was 100 W and 20 W, respectively, and the corresponding deposition rate was 1.2 and 0.32 nm min$^{-1}$, respectively. As detailed in Refs. [25–27], these deposition parameters ensured that LSCF was dense, crack-free, and highly granular. Both LSCF and YSZ thin films were under compressive stresses during device fabrication and fuel cell operation. Annealing in wet 5% $H_2$ was performed in a closed chamber at a flow rate of 0.1 L min$^{-1}$. The $H_2$ flow was maintained throughout the annealing until sample temperature fell below 100 °C. Annealing in air was conducted in a Thermolyne 21100 tube furnace. Ramping and cooling rates were both 10 °C min$^{-1}$ during the annealing. Grazing incidence X-ray diffraction (XRD) was performed with a Scintag 2000 diffractometer using Cu $K_\alpha$ radiation. Surface morphology was investigated by Carl Zeiss Ultra 55 field emission scanning electron microscopy (SEM). LSCF–YSZ interface was examined by JEOL 2100 transmission electron microscope (TEM). TEM samples were prepared by mechanical grinding, followed by $Ar^+$ ion-beam milling at 5 kV. Micrographs of membrane deformation were captured at automated intervals by a CCD camera (AmScope MD900E).

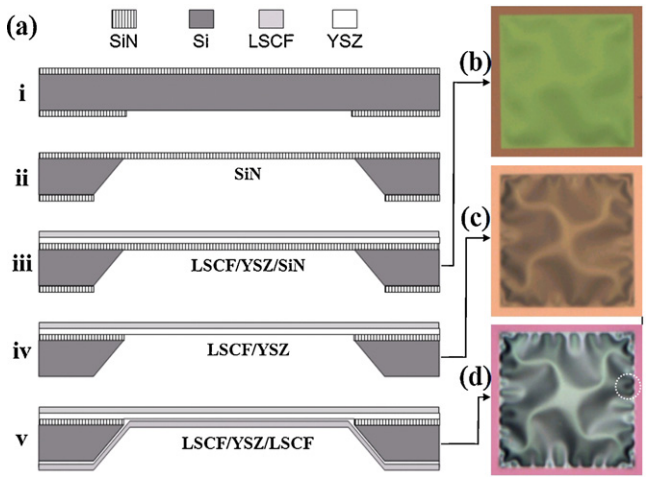


**Fig. 1.** (a) Fabrication procedure for LSCF-YSZ-LSCF μSOFCs. (b) Micrograph of a LSCF/YSZ/SiN membrane after step (iii). (c) Micrograph of a LSCF/YSZ membrane after step (iv). (d) Micrograph of a LSCF/YSZ/LSCF membrane after step (v). Nominal widths of the membranes are 160 μm. The dotted circle in (d) indicates a representative region on membrane–substrate boundaries that is highly susceptible to compressive stress induced cracking.

μSOFC membranes were fabricated on $Si_3N_4$-coated Si (SiN/Si) chips with dimension of 10 mm × 10 mm × 0.5 mm. The nominal width of square μSOFC membranes was 160 μm as measured by SEM. Fabrication procedures and the corresponding membrane deformation, which will be discussed in Section 3, are displayed in Fig. 1. In step (i), SiN thin films were patterned by photolithography and then removed by reactive ion etching (RIE). In step (ii), 30% KOH was used to etch through Si to release free standing SiN thin films from Si. In step (iii), 60-nm-thick YSZ and 65-nm-thick LSCF

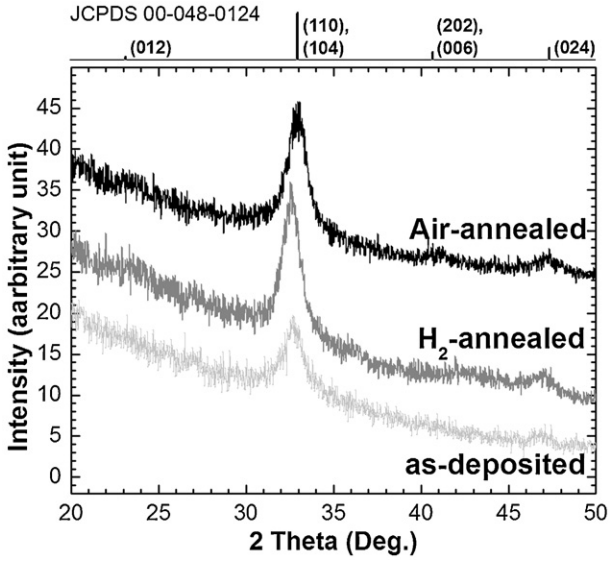


**Fig. 2.** XRD patterns of LSCF thin films that were as-deposited at 500 °C, annealed in flowing wet 5% $H_2$ at 550 °C for 10 h (referred to as $H_2$-annealed), and annealed in air at 550 °C for 10 h (referred to as air-annealed). Peak position and relative peak intensity of the macrocrystalline rhombohedral $La_{0.6}Sr_{0.4}Co_{0.8}Fe_{0.2}O_3$ indexed in JCPDS 00-048-0124 are presented on top of the plot.

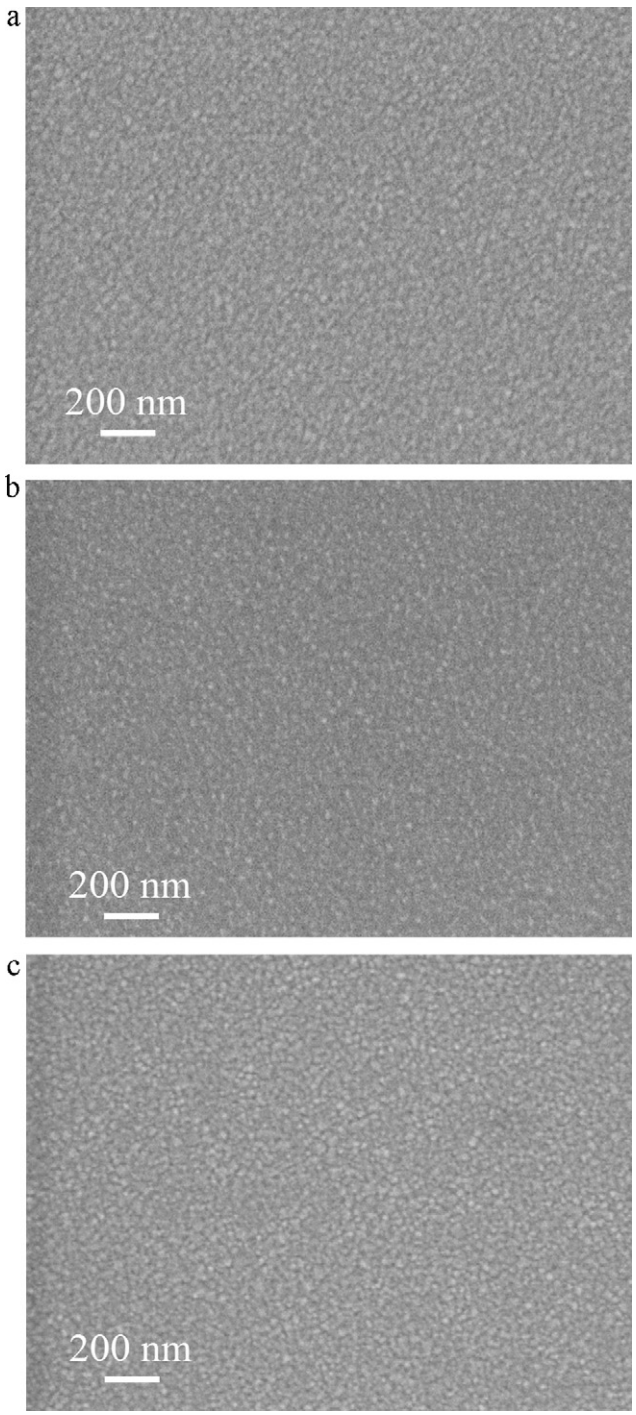


**Fig. 3.** High resolution SEM images of 65-nm-thick LSCF thin films that were (a) as-deposited at 500 °C, (b) annealed in flowing wet 5% $H_2$ at 550 °C for 10 h, and (c) annealed in air at 550 °C for 10 h. The substrates were single crystalline (1 0 0) YSZ.

were deposited onto the front side (i.e., the exposed side of SiN thin films prior to the processing) of the SiN membranes. In step (iv), RIE was used to remove SiN to release LSCF/YSZ thin films. In step (v), 5-nm-thick YSZ and then LSCF were deposited onto the back side, yielding LSCF/YSZ/LSCF (LYL) μSOFC membranes. The purpose of 5-nm-thick YSZ was to prevent the interfacial reaction between LSCF and Si [25]. Deposition parameters and time for the LSCF anodes were identical to that of the LSCF cathodes.

Fuel cell measurements were performed on as-fabricated LYL μSOFCs using the apparatus described in Ref. [6]. During the measurement, wet 5% $H_2$ forming gas was fed to the anode on the

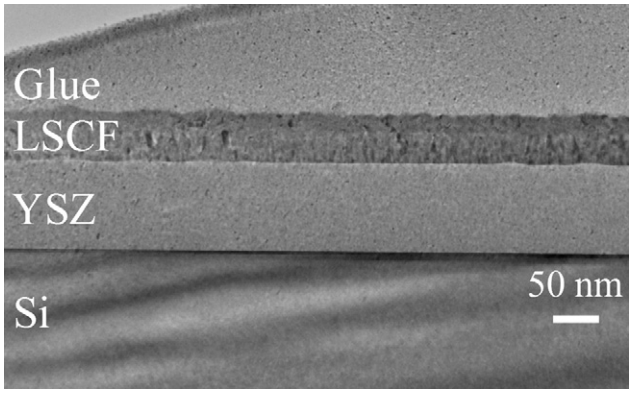


**Fig. 4.** Cross-sectional TEM image of LSCF grown on thin film YSZ electrolyte. The substrate was SiN-coated Si.

bottom of the chips while the top was exposed to air. No current collectors were implemented directly on the μSOFC membranes. On the top of the chip (cathode side), a micromanipulator probe was located close to the μSOFC membranes; silver (Ag) paste was painted on the bottom of the chip. Immediately after the fuel cell measurement, long-term stability testing was performed at 500 °C for 102 h while maintaining the probe contact and $H_2$ feeding. Micrographs of buckling deformation and OCV were obtained at automated intervals during the testing in situ.

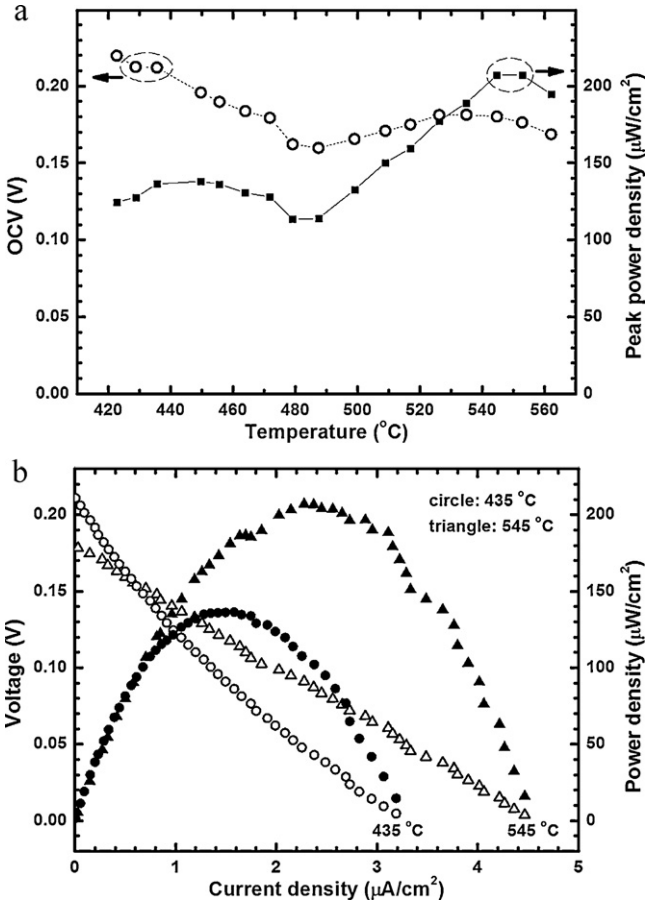


**Fig. 5.** (a) Temperature dependence of open circuit voltage (OCV) and peak power density (■) for a LSCF/YSZ/LSCF μSOFC. (b) Voltage (open symbols) and power density (solid symbols) as a function of current density at 435 °C (circular symbols) and 545 °C (triangular symbols).

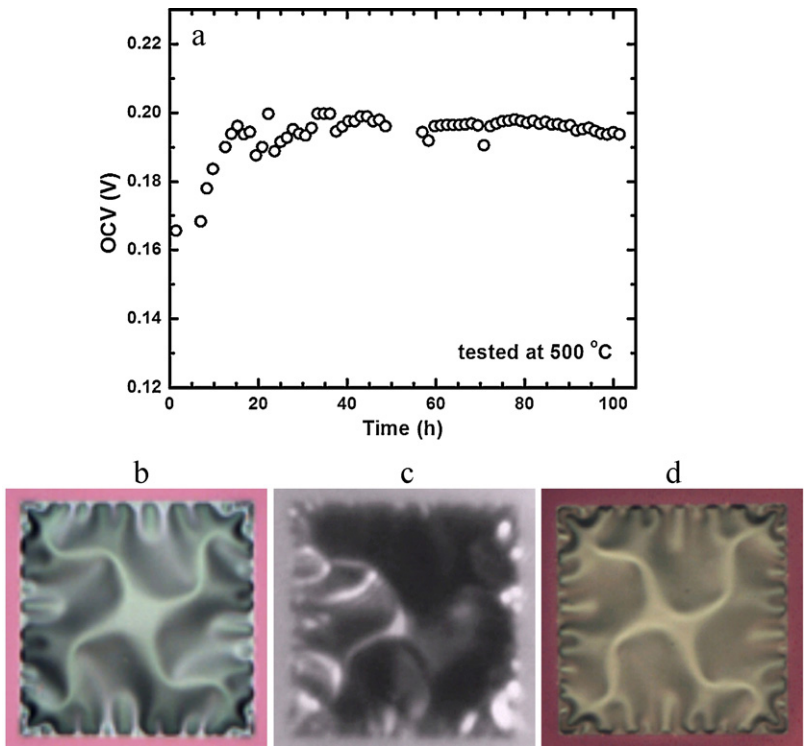


**Fig. 6.** (a) OCV as a function of elapsed time in the long-term stability testing at 500 °C. Micrographs of LSCF/YSZ/LSCF μSOFC membranes taken at (b) RT before the testing, (c) 500 °C after 15 h of testing, and (d) RT after 102 h of testing. Nominal widths of the membranes are 160 μm. Note that (b) is the same figure as Fig. 1(d).

## 3. Results and discussion

65-nm-thick LSCF thin films were deposited on single-crystalline YSZ (1 0 0) substrates at 500 °C (referred to as as-deposited LSCF) and then annealed at 550 °C for 10 h in 5% $H_2$ ambient (referred to as $H_2$-annealed LSCF) to investigate their lattice and microstructure stability in a reducing environment. The same as-deposited thin films were also annealed in air for 10 h (referred to as air-annealed LSCF). Fig. 2 shows XRD patterns of these three LSCF thin films. Position of (1 1 0) and (1 0 4) peak in the as-deposited LSCF is slightly lower than that listed in JCPDS 00-0480-0124 – namely, ~32.60° as compared to ~32.95° 2-theta – since the low oxygen partial pressure in the deposition environment (5 mTorr Ar) produces oxygen-deficient thin films. Oxygen deficiency in LSCF tends to increase unit cell volumes and lattice constants and thus lower peak positions in XRD patterns [32–34]. Therefore, after annealing in $H_2$ no apparent change in lattice constant was observed, as seen in Fig. 2, because the films remain highly oxygen deficient. In contrast, air-annealed LSCF exhibits similar peak positions as that in JCPDS 00-0480-0124 because of nearly stoichiometric oxygen content in LSCF. Fig. 2 also shows that, after annealing in $H_2$ and air, LSCF remains rhombohedral and there is no formation of any secondary phases. Surface morphology of the as-deposited, $H_2$-annealed, and air-annealed LSCF thin films are displayed in Fig. 3(a)–(c), respectively. As seen, the microstructures of these three thin films are all dense and crack-free. There is no significant difference in microstructures between the $H_2$- and air-annealed LSCF thin films. As detailed in Ref. [27] and evident in Fig. 1(b)–(d), these observations are likely due to the presence of compressive stresses inhibiting grain growth and crack formation in these substrate-clamped LSCF thin films.

To investigate the effect of $H_2$ and air annealing on the LSCF–YSZ interface, a 65-nm-thick LSCF thin film was deposited onto YSZ thin film-coated SiN-Si substrates at 500 °C. The film then underwent annealing in air for 2 h at 600 °C and in 5% $H_2$ for 2 h at 600 °C. After the annealing, no reaction layer was observed at the LSCF–YSZ interface, as seen in the cross-sectional TEM micrograph (Fig. 4). The micrograph also shows that YSZ and LSCF thin films are uniform in thickness and YSZ–SiN interface, LSCF–YSZ interface, and LSCF surface are all smooth. The absence of any crystalline interfacial reaction layer can also be verified in the XRD patterns shown in Fig. 2.

μSOFCs consisting of LSCF cathodes, YSZ electrolytes, and LSCF anodes were fabricated following the procedure listed in Fig. 1. The μSOFCs are square in shape, with nominal widths of 160 μm. Deformation of membranes during the fabrication is displayed in Fig. 1(b)–(d). No buckling was observed in SiN membranes after releasing from Si (step (ii)). Deposition of LSCF and YSZ (step (iii)) lead to buckled LSCF/YSZ/SiN membranes, as seen in Fig. 1(b), due to compressive stresses in bi-layer LSCF/YSZ thin films, as evident in Fig. 1(c). Details of stress state optimization in LSCF/YSZ membranes can be found in Ref. [27]. After depositing YSZ buffer layer and LSCF anodes onto the LSCF/YSZ membranes, additional compressive stresses and buckling deformation were introduced, as seen in Fig. 1(d). To accommodate differences in the dimensionality between supporting Si substrates and free-standing membranes, the membranes wrinkle in a quasi-periodic fashion along substrate-membrane boundaries. For highly buckled membranes, buckled regions similar to the one circled in Fig. 1(d) are mostly susceptible to buckling-induced cracking because they need to transition buckling deformation within a short length scale.

Temperature-dependent open circuit voltage (OCV) and peak power density of a LYL μSOFC is plotted in Fig. 5(a), while voltage and power density as a function of current density at selected temperatures are shown in Fig. 5(b). As seen in Fig. 5(a), the OCV is 0.22 V and peak power density reaches 125 μW $cm^{-2}$ at 420 °C. However, with increasing temperature, the OCV decreases in 420–490 °C range and then becomes relatively stable in 490–560 °C range. In contrast, the peak power density is relatively stable in 420–490 °C range and begins to increase at 490 °C until reaching

the maximum value of 210 μW cm$^{-2}$ at 545 °C. The unusual OCV behavior in 420–490 °C range is still not clear. A similar behavior was also observed in as-fabricated LSCF/YSZ/Pt μSOFCs when heated in 450–500 °C range [27].

At 550 °C, the OCV (~0.2 V) measured is much lower than the ideal OCV (~1.03 V) calculated from the Nernst equation for SOFCs using wet 5% $H_2$. We attribute this mainly to the resistive losses from LSCF anodes because current collectors were not used and LSCF possesses much lower electronic and ionic conductivities in a reducing environment than in an oxidizing environment [22,33]. Since electronic conductivity is low in reduced LSCF, the resistive loss is directly related to the electron transport that is along the following route: the reaction sites on the anode surface → LSCF anode surface → LSCF thin films on the side walls of 500-μm-deep etched wells → LSCF thin films on the bottom of the chip → external contact. Note that the shortest distance from the μSOFCs to the bottom of the chip is ~0.86 mm while that from the center of μSOFCs to the contact is in 1.5–3.5 mm range. The resistive loss induced OCV reduction was verified by two observations: OCV never exceeded 0.1 V when Ag paste was not painted on the bottom of the chip and OCV was 0.02 V lower when the manipulator probe was moved from close vicinity of μSOFC membranes to ~1.0 mm away from them.

It is important to emphasize that the performance of LYL μSOFCs (210 μW cm$^{-2}$ at 545 °C and 125 μW cm$^{-2}$ at 420 °C) is reasonably good based on the following two facts: (i) the power density of conventional SOFCs with catalytic oxide anodes [11,12] is typically few hundred mW cm$^{-2}$ at 900 °C and a temperature reduction of 200–300 °C could lower power density by two orders of magnitude [35,36]. In other words, to a first approximation, the power density of LYL μSOFCs is approximately one order of magnitude lower than that of well developed all-oxide SOFCs [11,12] scaled down to similar temperatures. The performance achieved by these LYL μSOFCs is encouraging when considering that these LYL μSOFCs were measured without current collectors on them. In fact, for other types of fuel cells such as proton exchange membrane fuel cells [37], performance that is two orders of magnitude lower is not unusual when using a novel Pt-free catalyst instead of commercially available Pt-based catalyst [38,39].

A remarkable aspect of LYL μSOFCs is the stability of OCV and buckling deformation during 100 h of testing at 500 °C (Fig. 6) and crack-free microstructure (Figs. 7 and 8) after the testing. Such long-term stability of μSOFCs has never been demonstrated previously to the best of our knowledge, mainly due to the microstructure instability of commonly porous Pt anode. As seen in Fig. 6(a), OCV reaches a plateau after 15 h of testing at 500 °C and is stable for the rest of the testing. Despite the fact that thermal expansion coefficients of LSCF and YSZ are greater than that of the supporting Si, a striking similarity in buckling deformation of LYL μSOFCs was observed before, during, and after the measurement and testing, as evident in Fig. 6(b)–(d). It indicates that the compressive stress-induced buckling is initially at a stable state. As discussed in our previous reports [27,40] on LYP μSOFCs (i.e., when Pt is used as the anode), stress changes at high temperatures include microstructure change of porous Pt thin films due to agglomeration, and strain gradient along the film thickness direction due to difference in initial film stresses and thermal expansion between LSCF cathode and Pt anode. These factors are essentially eliminated in the LYL μSOFC membranes in this report, leading to the remarkable buckling deformation stability of these μSOFCs. Note that Fig. 6(b) is the same figure as Fig. 1(d); it is placed alongside Fig. 6(c) and (d) for easier visual comparison of the buckling patterns.

After the long-term stability testing, microstructures of LSCF cathode and anode were carefully examined by high-resolution SEM. Fig. 7(a) shows the upper right corner of the membrane shown in Fig. 6(d). Close-up images of two selected regions in Fig. 7(a)

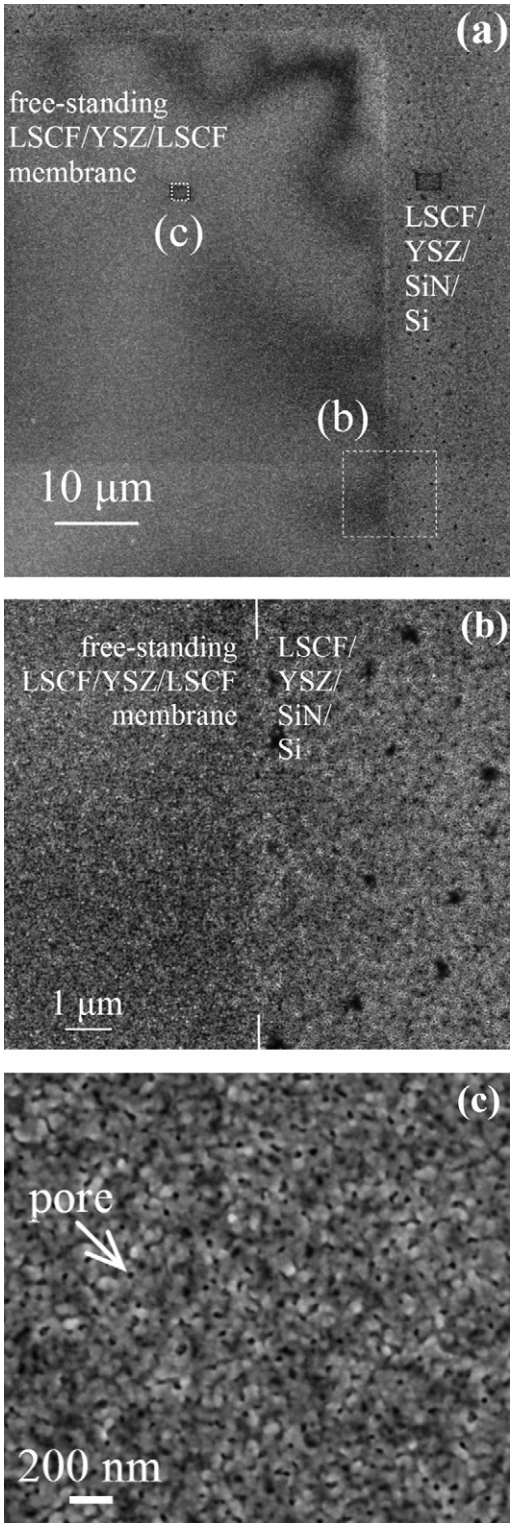


**Fig. 7.** High-resolution SEM images of LSCF cathode after 100-h long-term stability testing. (a) Upper right corner of the LSCF/YSZ/LSCF membrane shown in Fig. 6(d). (b) Crack-free microstructure of LSCF cathode in the vicinity of membrane–substrate boundaries. (c) Nano-porous, crack-free microstructure of LSCF cathode on free-standing LSCF/YSZ/LSCF membranes. Solid white lines are used to indicate the membrane–substrate boundaries in (b).

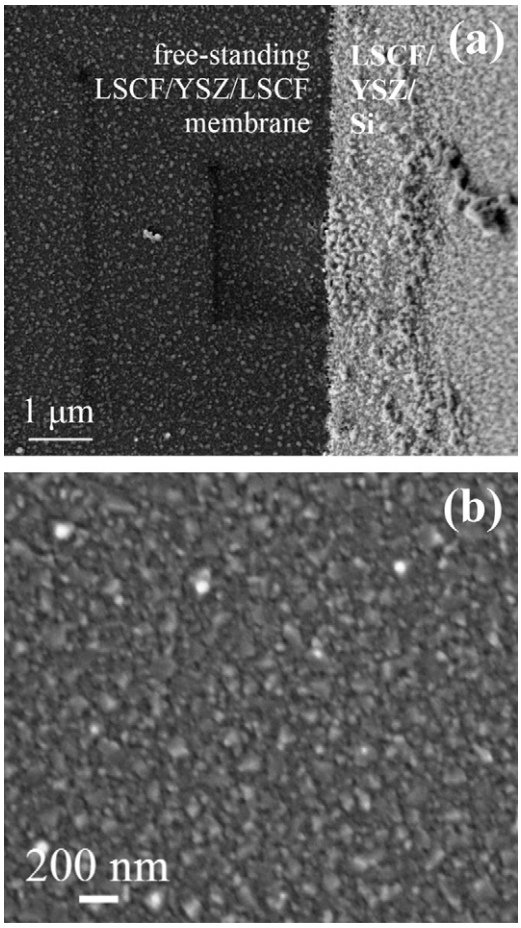


**Fig. 8.** High-resolution SEM images of LSCF anode after 100-h long-term stability testing. (a) Crack-free microstructure of LSCF anode in the vicinity of membrane–substrate boundaries. (b) Crack-free microstructure of LSCF anode on free standing LSCF/YSZ/LSCF membranes.

are displayed in Fig. 7(b) and (c). As seen in Fig. 7(a) and (b), the membrane–substrate boundaries are barely discernible because there is no apparent difference in microstructure between the LSCF on free-standing membranes and the LSCF clamped on the substrate. Absence of cracks or their traces is evident in Fig. 7(b) and (c). Interestingly, after prolonged high temperature testing, small pores are formed on the LSCF cathodes. We speculate that the pores might be linked to the OCV increase during this long term stability testing. Similar to the cathode, the LSCF anode is also free of cracks (Fig. 8(a)). However, the LSCF anode does not form pores (Fig. 8(b)), indicating that the microstructure of LSCF anode (Figs. 3(c) and 8(b)) is more stable than that of LSCF cathode (Figs. 3(b) and 7(c)). This phenomenon is attributed to the lattice structure of LSCF anode being more stable (as evident in Fig. 2). Since the pores are not observed in air-annealed LSCF thin films on YSZ (Fig. 3(b)) and 100-h-treated LSCF anode on μSOFCs (Fig. 8(b)), it is likely that the combination of lattice change and current flow during the long-term testing is responsible for the subtle microstructure change in LSCF cathode.

Here, we point out a difference between the LSCF anodes used in conventional SOFCs [17,18,21–23] and in our micro-SOFCs regarding thermomechanical instability [21]. In the former case, the LSCF anode is mostly synthesized at temperatures higher than 1000 °C in an oxidizing environment; the resulting fuel cells are typically operated at temperatures above 800 °C [17,18] in a reducing environment. As the result, the LSCF could experience apparent changes in lattice structure, microstructure, and interface, leading to potential thermomechanical instability [21] issues. In contrast, the LSCF thin films synthesized and operated at lower temperatures may avoid such issues. Moreover, as suggested by Sin et al. [18], thinner LSCF films in μSOFCs are likely more redox stable than their thicker counterparts in conventional SOFCs.

The results presented in this report indicate that the LSCF deposited in a vacuum environment is encouraging for anode applications because of its stable lattice structure in reducing environment and stable buckling deformation and crack-free microstructure after the long-term stability testing. Compared to conventional all-oxide SOFCs using LSCF anodes [17,18] or other catalytic oxide anodes [11,12], performance of the LYL μSOFCs in this report is encouraging with room for further improvement. The results and discussion in this report indicate that there are several approaches that potentially can further enhance the performance of all-oxide μSOFCs. Using membrane-supporting metal grids [41,42] on the anode side and/or thinner Si substrates could reduce the resistive losses that are associated with electronic transport; while porous oxide electrodes could possibly further improve OCV. We anticipate the results will motivate further research in Pt-alternatives and oxide anodes for thin film-based solid oxide fuel cells.

## 4. Conclusions

We have investigated symmetric thin film LSCF/YSZ/LSCF μSOFCs. The LSCF anodes exhibit stable microstructure and interface with YSZ in a reducing environment. Compared to μSOFCs with Pt anodes, the LSCF-YSZ-LSCF μSOFCs display good thermomechanical stability and crack-free microstructure after over 100 h of long-term stability testing at 500 °C. Peak power density and open circuit voltage of such all-oxide μSOFCs at 420 °C are 125 μW cm$^{-2}$ and 0.22 V, respectively; while that at 545 °C are 210 μW cm$^{-2}$ and 0.18 V, respectively. The study could be relevant towards further advancing low temperature solid oxide fuel cells using thin film components.

## Acknowledgment

The authors acknowledge National Science Foundation for financial support.

## References

[1] A. Bieberle-Hutter, D. Beckel, A. Infortuna, U.P. Muecke, J.L.M. Rupp, L.J. Gauckler, S. Rey-Mermet, P. Muralt, N.R. Bieri, N. Hotz, M.J. Stutz, D. Poulikakos, P. Heeb, P. Muller, A. Bernard, R. Gmur, T. Hocker, J. Power Sources 177 (2008) 123–130.
[2] X. Chen, N.J. Wu, L. Smith, A. Ignatiev, Appl. Phys. Lett. 84 (2004) 2700–2702.
[3] H. Huang, M. Nakamura, P.C. Su, R. Fasching, Y. Saito, F.B. Prinz, J. Electrochem. Soc. 154 (2007) B20–B24.
[4] A. Ignatiev, X. Chen, N.J. Wu, Z.G. Lu, L. Smith, Dalton Trans. 40 (2008) 5501–5506.
[5] A.F. Jankowski, J.P. Hayes, R.T. Graff, J.D. Morse, Mater. Res. Soc. Symp. Proc. 730 (2002), V4.2.1.
[6] A.C. Johnson, B.-K. Lai, H. Xiong, S. Ramanathan, J. Power Sources 186 (2009) 252–260.
[7] X.H. Wang, H. Huang, T. Holme, X. Tian, F.B. Prinz, J. Power Sources 175 (2008) 75–81.
[8] A. Atkinson, S. Barnett, R.J. Gorte, J.T.S. Irvine, A.J. McEvoy, M. Mogensen, S.C. Singhal, J. Vohs, Nat. Mater. 3 (2004) 17–27.
[9] S. McIntosh, R.J. Gorte, Chem. Rev. 104 (2004) 4845–4865.
[10] Y.-H. Huang, R.I. Dass, Z.-L. Xing, J.B. Goodenough, Science 312 (2006) 254–257.
[11] S. Tao, J.T.S. Irvine, Nat. Mater. 2 (2003) 320–323.
[12] Y. Zheng, C. Zhang, R. Ran, R. Cai, Z. Shao, D. Farrusseng, Acta Mater. 57 (2009) 1165–1175.
[13] X. Li, H. Zhao, N. Xu, X. Zhou, C. Zhang, N. Chen, Int. J. Hydrogen Energy 34 (2009) 6407–6414.
[14] J.B. Goodenough, Y.H. Huang, J. Power Sources 173 (2007) 1–10.

[15] R. Doshi, C.B. Alcock, N. Gunasekaran, J.J. Carberry, J. Catal. 140 (1993) 557–563.
[16] R.J.H. Voorhoeve, D.W. Johnson, J.P. Remeika, P.K. Gallagher, Science 195 (1977) 827–833.
[17] J.C. Fisher, S.S.C. Chuang, Catal. Commun. 10 (2009) 772–776.
[18] A. Sin, E. Kopnin, Y. Dubitsky, A. Zaopo, A.S. Arico, L.R. Gullo, D.L. Rosa, V. Antonucci, J. Power Sources 145 (2005) 68–73.
[19] U. Balachandran, J.T. Dusek, R.L. Mieville, R.B. Poeppel, M.S. Kleefisch, S. Pei, T.P. Kobylinski, C.A. Udovich, A.C. Bose, Appl. Catal. Gen. 133 (1995) 19–29.
[20] P. Tsiakaras, C. Athanasiou, G. Marnellos, M. Stoukides, J.E. ten Elshof, H.J.M. Bouwmeester, Appl. Catal. Gen. 169 (1998) 249–261.
[21] M. Weston, I.S. Metcalfe, Solid State Ionics 113–115 (1998) 247–251.
[22] S. Tao, J.T.S. Irvine, Solid Oxide Fuels Cells VIII (SOFC VIII), Electrochemical Society, Pennington, NJ, USA/Paris, France, 2003.
[23] A. Hartley, M. Sahibzada, M. Weston, I.S. Metcalfe, D. Mantzavinos, Catal. Today 55 (2000) 197–204.
[24] T. Cain, B.-K. Lai, S. Sankaranarayanan, S. Ramanathan, J. Power Sources (2009).
[25] B.K Lai, H. Xiong, M. Tsuchiya, A.C. Johnson, S. Ramanathan, Fuel Cells 9 (2009) 699–710.
[26] B.-K. Lai, A.C. Johnson, H. Xiong, S. Ramanathan, J. Power Sources 186 (2009) 115–122.
[27] B.-K. Lai, K. Kerman, S. Ramanathan, J. Power Sources 195 (2010) 5185–5196.
[28] H. Xiong, B.-K. Lai, A.C. Johnson, S. Ramanathan, J. Power Sources 193 (2009) 589–592.
[29] V.T. Srikar, K.T. Turner, T.Y.A. Ie, S.M. Spearing, J. Power Sources 125 (2004) 62–69.
[30] Y.H. Tang, K. Stanley, J. Wu, D. Ghosh, J.J. Zhang, J. Micromech. Microeng. 15 (2005) S185–S192.
[31] N. Yamamoto, D.J. Quinn, N. Wicks, J.L. Hertz, J. Cui, H.L. Tuller, B.L. Wardle, J. Micromech. Microeng. 20 (2010) 035027.
[32] L.-W.T.M.M. Nasrallah, H.U. Anderson, D.M. Sparlin, S.R. Sehlin, Solis State Ionics 76 (1995) 259–271.
[33] S. Wang, M. Katsuki, M. Dokiya, T. Hashimoto, Solid State Ionics 159 (2003) 71–78.
[34] M. Katsuki, S. Wang, M. Dokiya, T. Hashimoto, Solid State Ionics 156 (2003) 453–461.
[35] Z.P. Shao, S.M. Haile, Nature 431 (2004) 170–173.
[36] A. Yan, M. Cheng, Y.L. Dong, W.S. Yang, V. Maragou, S.Q. Song, P. Tsiakaras, Appl. Catal. B: Environ. 66 (2006) 64–71.
[37] J.-H. Wee, K.-Y. Lee, S.H. Kim, J. Power Sources 165 (2007) 667–677.
[38] A.L. Goff, V. Artero, B. ousselme, P.D. Tran, N. uillet, R. Métayé, A. Fihri, S. Palacin, M. Fontecave, Science 326 (2009) 1384–1387.
[39] S. Woloshin, L.M. Schwartz, B.S. Kramer, Nature 462 (2009) 701.
[40] B.-K. Lai, A. Johnson, H. Xiong, C. Ko, S. Ramanathan, Exploratory studies of on-chip solid oxide fuel cells incorporating ultra-thin nanostructured platinum and cerium oxide films as anode components, in: S. Luryi, J. Xu, A. Zaslavsky (Eds.), Future Trends in Microelectronics, Wiley-IEEE Press, New York, 2010, pp. 411–422.
[41] A. Johnson, A. Baclig, D.V. Harburg, B.-K. Lai, S. Ramanathan, J. Power Sources 195 (2010) 1149–1155.
[42] S. Rey-Mermet, P. Muralt, Solid State Ionics 179 (2008) 1497–1500.